ACS OMEGA

http://pubs.acs.org/journal/acsodf

Article

# Formation of Novel Bimetal Oxide $In_2V_2O_7$ through a Shock Compression Method

Xin Gao, Haotian Ran, Qiang Zhou, Toshimori Sekine, Jianjun Liu, Yan Chen, and Pengwan Chen*

Cite This: *ACS Omega* 2022, 7, 27602−27608

Read Online

ACCESS | Metrics & More | Article Recommendations

**ABSTRACT:** Bimetal oxides with a chemical formula of $A_2B_2O_7$ have received much attention from plenty of research groups owing to their outstanding properties, such as electronic, optical, and magnetic properties. Among the abundant element combinations of cations A and B, some theoretically predicted compounds have not successfully been synthesized in experiments, such as $In_2Zr_2O_7$, $In_2V_2O_7$, etc. In this study, a novel tetragonal pyrochlore-like $In_2V_2O_7$ nanopowder has been reported for the first time. $In_2O_3$ and $VO_2$ powders mixed through ball milling were reacted to form $In_2V_2O_7$ by shockwave loading. The recovered sample is investigated to be nanocrystalline $In_2V_2O_7$ powder through various techniques, such as X-ray diffraction, scanning electron microscopy, X-ray energy spectrum analysis, and transmission electron microscopy. The formed $In_2V_2O_7$ is indexed as a tetragonal cell with $a = b = 0.7417$ nm and $c = 2.1035$ nm. Moreover, the formation mechanism of $In_2V_2O_7$ through a shock synthesis process is carefully analyzed based on basic laws of shockwave. The experimental results also confirm that a high shock temperature and high shock pressure are the two key factors to synthesize the $In_2V_2O_7$ nanopowder. Our investigation demonstrates the high potential application of a shock-induced reaction on the synthesis of novel materials, including the preparation of new bimetal oxides.

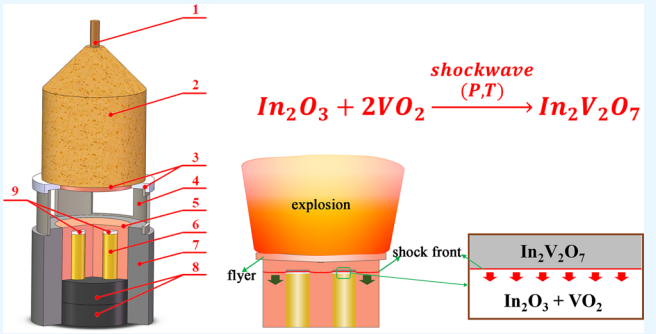


## INTRODUCTION

The human quest for new and exotic materials has given thrust to the research on materials science, urging researchers to focus on creating (exploring) materials with exotic properties by disturbing their original electronic structure using various external parameters such as pressure and/or temperature.[1]

Among plenty of materials, bimetal oxides are important functional semiconductor materials featuring low cost and outstanding properties owing to the coupling effect of two metal elements.[2−4] With respect to the bimetal oxide with a general formula of $A_2B_2O_7$, coupling effects lead to their various applications,[5−8] including multiferroics,[9,10] radiation resistance,[11] high-temperature heating materials,[12] sensors,[13,14] fuel cell electrode materials,[14,15] nuclear waste solidification,[16] and photocatalytic materials.[17−20] Transition metal vanadate nanomaterials are important functional materials owing to their fascinating structures and outstanding properties, such as electronic,[21,22] optical,[21,23] catalytic,[24] and magnetic properties.[25,26]

Since Ye et al.[27] reported the high photocatalytic performance of monoclinic phase $InVO_4$-III semiconductors, the indium vanadate materials have attracted the attention of many research groups. Because of their narrow band gap, suitable redox potential, and wide corresponding light range, indium vanadates, such as $InVO_4$ and $InVO_3$, possess good application prospect in photocatalytic decomposition of water to produce hydrogen,[27] for photocatalytic degradation of organic pollutants,[28] and as sensor materials.[29,30] Several methods have been applied to prepare indium vanadate materials, including a high-temperature solid-state method,[27] hydrothermal method,[31] sol−gel method,[32] spray pyrolysis,[33] electrospinning method,[34] etc. Through the above methods, $InVO_4$ and $InVO_3$ are obtained by mixing precursors and inducing a synthetic reaction at certain temperatures with normal pressure. Synthesis of indium vanadate at a high pressure has rarely been reported. Based on previous research studies on bimetal oxide with the $A_2B_2O_7$ formula, the radii of $In^{3+}$ and $V^{4+}$ are suitable to synthesize $In_2V_2O_7$ in theory.[5] However, in spite of the suitable ionic radii, the corresponding pyrochlore oxide could not be stabilized under normal pressure synthesis conditions. High pressure techniques have been used to prepare pyrochlore-type materials. For example, the

Received: May 24, 2022
Accepted: July 19, 2022
Published: July 27, 2022







https://doi.org/10.1021/acsomega.2c03220
*ACS Omega* 2022, 7, 27602−27608

formation pressure to synthesize $Mn_2V_2O_7$ is 7 GPa[35] through a static high pressure method. However, the research corresponding to the synthesis of $In_2V_2O_7$ has not been reported through a high-pressure synthesis method or other methods.

Shock compression technology features a high dynamic pressure, high temperature, high quenching rate, etc.[36] Thus, it is utilized to process materials with large volume compared with static compression technology. Through this technology, the shockwave acts on a target material to generate ultrahigh pressures ($10^0$–$10^2$ GPa) and temperatures ($10^2$–$10^4$ K) in microseconds, inducing multiple physical and chemical phenomena. Consequently, shock loading approaches have been widely applied in various material processing fields, such as metallic material hardening,[37−39] material doping,[40] synthesis of novel materials,[41−43] shock-induced phase transformation,[44,45] and shock activation of materials.[46] With respect to this method, several techniques have been developed to adjust the pressure and temperature during shock compression for the synthesis of materials, such as organic molecules using inorganic precursors,[47] nanodiamonds,[48] doped $TiO_2$,[49] and doped graphene.[43] Recently, a shock-induced chemical reaction has been applied to prepare bimetal oxide materials, such as $Gd_2Zr_2O_7$,[50] $La_2Ti_2O_7$,[36] etc.

This study presents the synthesis of novel bimetal oxide, $In_2V_2O_7$ nanopowder, through a shock-induced chemical reaction using $In_2O_3$ and $VO_2$ powders as precursors. The experimental results demonstrate that a high shock pressure and high shock temperature are the two critical factors to improve the formation of $In_2V_2O_7$ through this method.

## EXPERIMENTAL PROCEDURES

In the experiments, a copper recovery device was designed with three circumferentially uniformly distributed sample holes with a diameter of 10 mm and depth of 1 mm (see Figure 1).

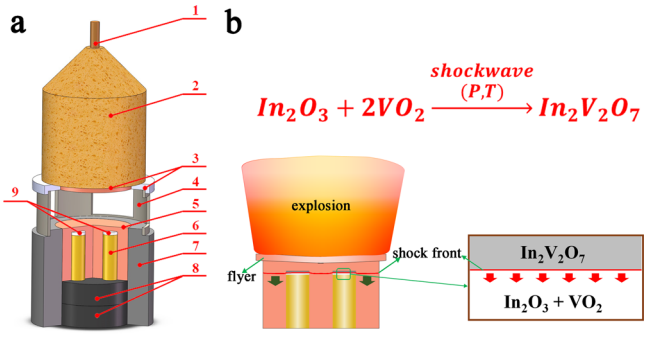


**Figure 1.** (a, b) Schematic of shock compression assembly. 1: detonator, 2: detonation lens and main charge, 3: flyer and flyer cover, 4: PVC surpport, 5: sample recovery device, 6: copper plug, 7: steel base, 8: momentum-trap blocks, and 9: precursor.

The precursor powder, a mixture of $In_2O_3$ and $VO_2$ powders with a mole ratio of 1:2, was activated through ball milling treatment for 6 h. The corresponding conditions include a milling ball material of zirconia, milling speed of 750 r/min, and ball milling medium of 20 g of ethanol and helium gas. Subsequently, the activated precursor powder was filled into the sample holes with a certain initial density ($\rho_{00}$, identified as the ratio of precursor mass to sample hole volume) and blocked by a copper plug.

Then, the sample recovery device with a flyer, a main charge, and other devices was assembled, as shown in Figure 1. The detonation lens and main charge (a mixture of RDX and a polymer binder with a detonation velocity of 8315 m/s) were applied to accelerate the copper flyer. Then, the flyer impacts on the sample recovery device to generate a high temperature and high pressure in the precursor to synthesize $In_2V_2O_7$. In this experiment, the different initial relative densities of precursor powder ($\rho_{00}/\rho$, in which $\rho$ is the theoretical density of the precursor powder) were used to adjust the shock temperature owing to the adiabatic process during shock loading. In general, a low relative density leads to a stronger adiabatic compression, inducing a higher shock temperature. In addition, the impact velocity ($v$) was used to adjust the shock pressure. The corresponding experimental conditions are listed in Table 1. After shock experiments, the shock-treated samples were recovered for further characterization.

**Table 1. Experimental Conditions for Shock Loading on Precursor Powders**[a]

| no. | ball mill time (h) | $\rho_{00}$ (g·cm$^{-3}$) | $\rho_{00}/\rho$ | $v$ (km·s$^{-1}$) | $p$ (GPa) | $I_{In2O3}$:$I_{new}$ |
|---|---|---|---|---|---|---|
| 1 | 6 | 5.178 | 0.91 | 2.2 | 54.7 | 557:100 |
| 2 | | 3.755 | 0.66 | 2.2 | 54.7 | 79:100 |
| 3 | | 2.333 | 0.41 | 2.2 | 54.7 | 65:100 |
| 4 | 6 | 5.235 | 0.92 | 3.2 | 90.3 | 1042:100 |
| 5 | | 3.642 | 0.64 | 3.2 | 90.3 | 21:100 |
| 6 | | 2.219 | 0.39 | 3.2 | 90.3 | 0:100 |

[a] $\rho_{00}$ is the initial density, $\rho_{00}/\rho$ is the initial relative density, $v$ is the impact velocity, $p$ is the shock pressure. $I_{In2O3}$:$I_{new}$ is the intensity ratio of the XRD peak at 31.8° (strongest peak of the new phase) to that of $In_2O_3$.

Considering the 1 mm thickness of precursor powder in the sample holes, the shockwave reflects at the device−precursor interface and precursor−plug interface repeatedly to increase the pressure and temperature in the precursor powder and induce the chemical reaction during the shock process.

The impact velocity ($u_{max}$) values were calculated according to the Gürney equation[51]

$$u_{max} = D\left[1 - \frac{1}{\eta}\left(\sqrt{1 + 2\eta} - 1\right)\right] \quad (1)$$

$$\eta = \frac{16\rho_0 l}{27\rho_M d} \quad (2)$$

where $D$ is the detonation velocity of the explosive, $\rho_0$ is the density of the explosive, $l$ is the height of the main charge, $\rho_M$ is the flyer density, and $d$ is the flyer thickness.

In the calculation of shock pressure, the mixed precursors were treated as a thin wafer (1 mm thick) enclosed by copper. After the impact induced by the shock-driven flyer, the generated shockwave reflects at the upper and lower interface between the thin precursor wafer and surrounding copper repeatedly, leading to the increase in shock pressure in the precursor. After multiple reflections, the shock pressure in the precursor reaches the pressure at the interface between the copper box and flyer. The shock pressure values were calculated based on the impedance match method. The detailed calculation process has been explained in 36 and 51.



https://doi.org/10.1021/acsomega.2c03220
ACS Omega 2022, 7, 27602−27608

The corresponding experimental parameters and calculated results are listed in Table 1.

The X-ray diffraction (XRD) patterns of the recovered samples were recorded by operating a BRUKER D8 at a working voltage of 40 kV and a working current of 40 mA with Cu K$\alpha$ radiation. The phase analysis and content of recovered samples were investigated through XRD results. The microstructures and morphology of samples were characterized by using a Tecnai $G^2$ F30 transmission electron microscope (TEM) with an accelerating voltage of 300 kV and a HITACHI S4800 scanning electron microscope (SEM), respectively. The chemical composition was further probed by XPS analysis using a Thermo ESCALAB 250 Xi spectrometer with a monochromatic AlK (1486.6 eV) X-ray source. The obtained XPS spectra were fit with nonlinear Shirley background correlation.

## RESULTS AND DISCUSSION

Figure 2 shows the XRD patterns of the ball-milled precursor ($M_0$) and the recovered Nos. 1−6 samples, revealing the presence of $In_2O_3$, $VO_2$, and copper and several XRD peaks of a new phase. The copper XRD peaks in Nos. 2−6 samples are from the copper fragments of the copper sample recovery device. The XRD pattern of the ball-milled precursor presents characteristic peaks at 21.5, 27.8, 30.5, 35.5, 37.8, 39.8, 45.6, 51.0, and 60.7°, showing the presence of $In_2O_3$ and $VO_2$. It indicates that ball milling treatment can hardly lead to the chemical reaction of $In_2O_3$ and $VO_2$ under the conditions in these experiments.

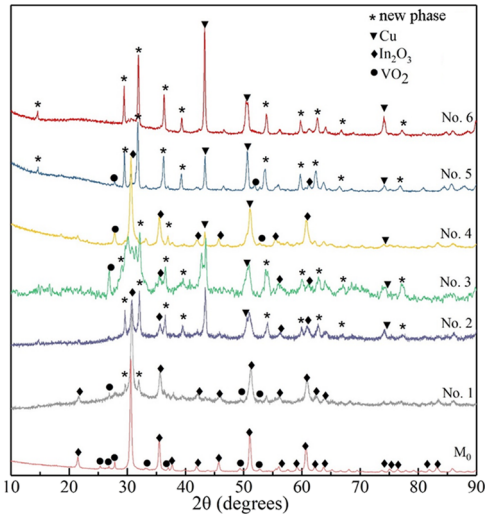


**Figure 2.** XRD patterns of ball-milled precursor powder and recovered Nos. 1−6 samples.

With respect to the XRD results of recovered samples, besides the peaks of $In_2O_3$, $VO_2$, and copper, several XRD peaks are observed at 14.6, 29.4, 36.3, 39.3, 53.9, 59.7, 62.6, 66.8, and 77.2°. These peaks are not matched with the known phases, implying the formation of a new phase through the shock loading process. Note that the peak positions and relative intensity values of the corresponding peaks are the same for the recovered samples (Nos. 2, 3, 5, and 6 samples, see Table 2), suggesting that the formed new phase should be the same in these shock experiments.

The XRD pattern of No. 1 sample presents two new peaks at 29.4 and 31.8°, implying the formation of the new phase. The XRD patterns of Nos. 1−3 samples show that the increase in shock temperature leads to more new XRD peaks with higher intensities in the XRD patterns. Based on the XRD patterns, the intensity ratio of the strongest peak of $In_2O_3$ to that of the new phase (peak at 31.8°) (see Table 1) is used to estimate the content of the new phase in recovered samples approximately. The intensity ratios of recovered samples suggest that the decrease in the initial relative density (corresponding to a higher shock temperature) can enhance the new phase content in recovered samples. In addition, under the same initial relative density, a higher impact velocity (corresponding to a higher shock pressure) also increases the new phase content in recovered samples by comparing Nos. 1−3 samples and Nos. 4−6 samples. With respect to the XRD pattern of No. 6 sample, there are only XRD peaks of copper and the new phase, implying that, at higher shock pressures (90 GPa) and temperatures, all precursor reacts to form the new phase compound.

Furthermore, Table 2 and Figure 3 also show the results of normalized peak intensity of the new phase with the peak at 31.86° as the standard XRD peak, revealing the high consistency of the relative intensity of corresponding peaks. Based on the above XRD results, it is assumed that the shock loading leads to the chemical reaction of $In_2O_3$ and $VO_2$ under a high shock temperature and pressure. The higher temperature and pressure enhance the yield of the formed new phase.

**Table 2. Peak Positions and Relative Intensities from XRD Patterns of Nos. 2, 3, 5, and 6 Samples**

| | no. 2 | | no. 3 | | no. 5 | | no. 6 | |
|---|---|---|---|---|---|---|---|---|
| peak number | 2$\theta$ (°) | $I$ (%) | 2$\theta$ (°) | $I$ (%) | 2$\theta$ (°) | $I$ (%) | 2$\theta$ (°) | $I$ (%) |
| 1 | | | | | 14.63 | 7.52 | 14.59 | 8.68 |
| 2 | 29.47 | 49.90 | 29.47 | 51.30 | 29.50 | 51.23 | 29.44 | 49.84 |
| 3 | 31.79 | 100.00 | 31.83 | 100.00 | 31.81 | 100.00 | 31.86 | 100.00 |
| 4 | 36.33 | 50.11 | 36.35 | 50.61 | 36.32 | 49.21 | 36.36 | 52.89 |
| 5 | 39.29 | 21.92 | 39.32 | 22.01 | 39.33 | 21.76 | 39.38 | 21.86 |
| 6 | 46.71 | 6.34 | 46.62 | 6.03 | 46.58 | 6.23 | 46.66 | 6.59 |
| 7 | 53.88 | 30.39 | 53.91 | 30.20 | 53.69 | 29.89 | 53.94 | 30.55 |
| 8 | 59.79 | 21.14 | 59.77 | 21.05 | 59.75 | 20.88 | 59.81 | 21.38 |
| 9 | 61.29 | 6.35 | 61.25 | 6.19 | 61.22 | 6.12 | 61.22 | 6.59 |
| 10 | 62.76 | 22.41 | 62.69 | 22.38 | 62.62 | 21.98 | 62.65 | 22.51 |
| 11 | 66.81 | 6.58 | 66.71 | 6.68 | 66.68 | 6.65 | 66.75 | 6.75 |
| 12 | 77.19 | 7.09 | 77.23 | 7.21 | 77.12 | 7.11 | 77.29 | 7.23 |



https://doi.org/10.1021/acsomega.2c03220
ACS Omega 2022, 7, 27602−27608

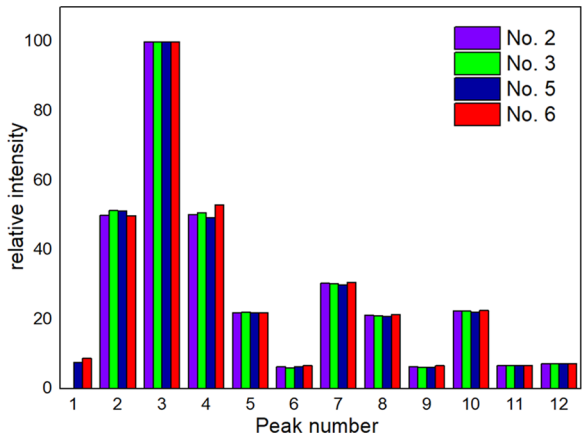


**Figure 3.** Relative peak intensities from XRD patterns.

Under proper conditions (No. 6 sample), the mixed precursor reacted completely to form the pure new phase.

Typical TEM images of No. 6 sample (Figure 4a) show quasi-spherical nanoparticles in sizes of 50−100 nm. The

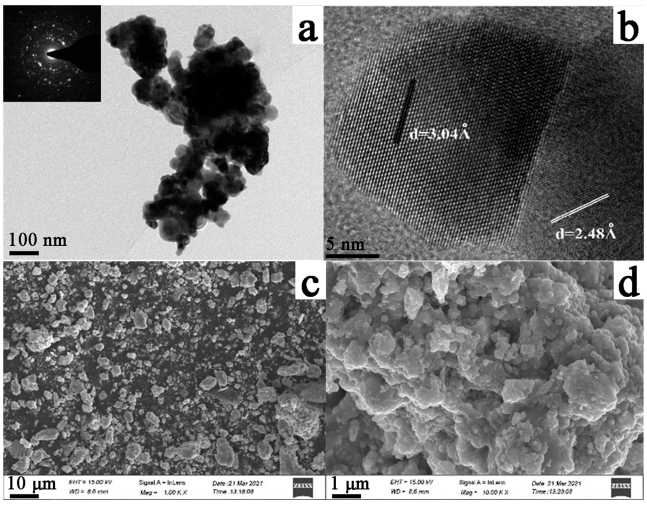


**Figure 4.** TEM and SEM imagines of No. 6 sample. (a) TEM and (b) HRTEM images of No. 6 sample. (c) SEM and (d) high-magnification SEM images of No. 6 sample.

corresponding high-resolution TEM (HRTEM) (Figure 4b) further reveals the nanocrystalline structure with high crystallinity. The corresponding *d*-spacing values from Figure 4b are 3.04 and 2.48 Å, respectively, which are in accordance with the XRD peaks at $2\theta = 29.4$ and 36.3° of the new phase. It also confirms the presence of new phase nanoparticles in No. 6 sample. Furthermore, the inset of Figure 4a presents the SAED patterns of the recovered samples, showing several ring-like diffraction patterns with dispersed bright spots, which indicate the presence of highly crystalline multiple crystals in the recovered samples. The TEM results are in good agreement with the XRD results, indicating the formation of the new phase induced by shock loading. Typical SEM images of No. 6 sample powder (Figure 4c,d) reveal the presence of agglomeration of formed new phase nanoparticles, which are mostly in a quasi-spherical shape with a size of 50−100 nm. In addition, the observed quasi-spherical particles imply that the melting phenomenon is generated by the shock-induced high temperature.

For further characterization, EDS is applied to confirm the elemental ratio of the new phase. The dot mapping EDS (see Figure 5a) shows that three elements (In, V, and O) are

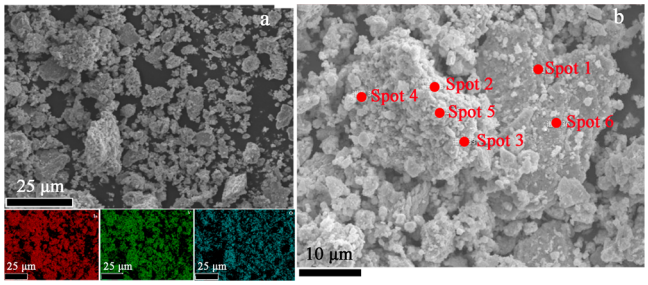


**Figure 5.** EDS results of No. 6 sample: (a) dot-mapping mode results and (b) spot mode results.

uniformly distributed in recovered samples. The corresponding general elemental ratio of In:V:O is 18.31:17.87:63.82, which is consistent with the element ratio of the precursor powder (In:V:O = 2:2:7). Considering that the majority of No. 6 sample is the formed new phase, the element ratio of In:V:O in the formed compound is supposed to be 2:2:7. Furthermore, all spot EDS results (see Figure 5b and Table 3) present that the element ratio of In:V:O in formed particles is 2:2:7 approximately, showing the elemental uniform distribution in the formed new phase. Consequently, the new phase revealed in the above characterization results is supposed to be one compound nanopowder with a chemical formula of $In_2V_2O_7$, which is different from the previous indium vanadates, e.g., $InVO_4$ and $InVO_3$.

Figure 6 presents the typical In 3d, V 2p, and O 1s XPS spectra of No. 6 sample. The corresponding peaks appeared at approximately 444.7 eV in In 3d spectrum, 517.1 eV in V 2p spectrum, and 530.0 eV in O 1s spectrum, showing the presence of indium vanadate in No. 6 sample. Moreover, based on the XPS results, the atomic ratio of In:V:O is 1:0.98:3.52, confirming that the new phase is $In_2V_2O_7$. The XPS results also imply the element composition and ratio, which support the identification of $In_2V_2O_7$ in the recovered samples.

Based on the recorded XRD data, this new phase can be indexed as a pyrochlore-like tetragonal cell with $a = b = 0.7417$ nm, $c = 2.1035$ nm, and $V_{cell} = 1.157$ nm$^3$ using the X-cell program in Material Studio. The calculated cell parameters of the new phase are different from those of indium vanadates, e.g., $InVO_4$ and $InVO_3$, also indicating that a new structure of indium vanadate formed under shockwave loading.

As shown in Figure 1b, the formation mechanism of shock-synthesized $In_2V_2O_7$ is discussed as below. The $In_2O_3$ powder and $VO_2$ powder were mixed and activated using ball milling. Then, the mixed precursor powder was impacted by the shock-driven flyer. Shock loading leads to adiabatic compression in precursor powder, generating a high temperature of a few thousands of K and a high pressure of dozens of GPa. Consequently, the chemical reaction of precursors is triggered by this extreme condition to form tetragonal pyrochlore-like $In_2V_2O_7$ powder. The short duration (microseconds) of shock loading inhibits the growth of the $In_2V_2O_7$ crystal to form nanocrystals. In addition, the high cooling rate during unloading is conducive to preserve the formed nanocrystalline $In_2V_2O_7$. Thus, the majority of recovered $In_2V_2O_7$ nanoparticles are in sizes of 50−100 nm. The corresponding chemical reaction formula is shown in Figure 1b. Furthermore,


https://doi.org/10.1021/acsomega.2c03220
ACS Omega 2022, 7, 27602−27608

**Table 3. EDS Results of No. 6 Sample**

| | percentage (%) | | | | | | |
|---|---|---|---|---|---|---|---|
| element | dot-mapping | spot 1 | spot 2 | spot 3 | spot 4 | spot 5 | spot 6 |
| In | 18.31 | 19.31 | 18.00 | 19.06 | 19.5 | 19.19 | 17.95 |
| V | 17.87 | 19.37 | 19.19 | 18.77 | 17.04 | 18.56 | 17.52 |
| O | 63.82 | 61.32 | 62.81 | 62.17 | 63.46 | 62.25 | 64.53 |
| total | 100 | 100 | 100 | 100 | 100 | 100 | 100 |

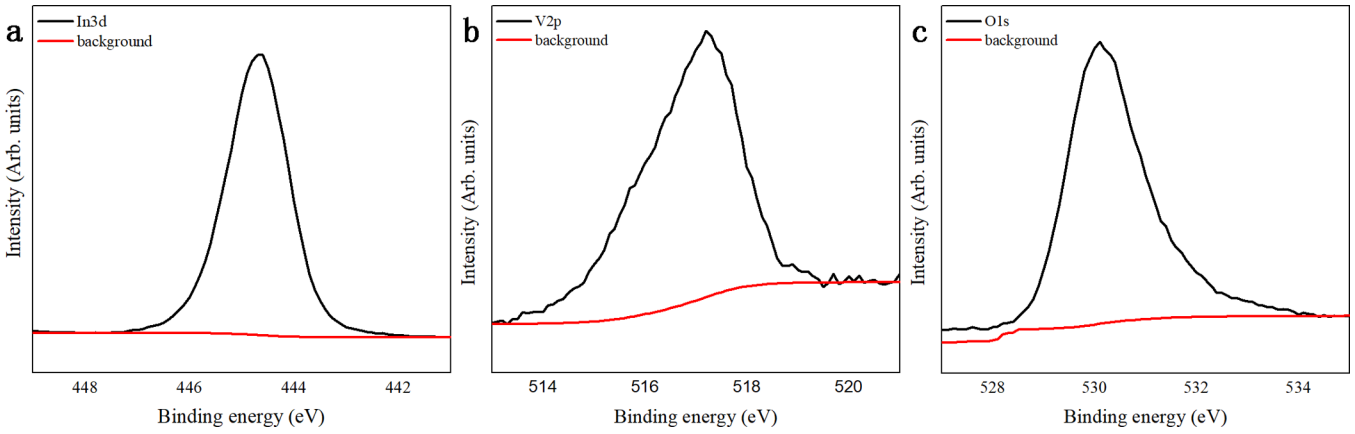


**Figure 6.** XPS spectra of No. 6 sample: (a) In 3d spectrum, (b) V 2p spectrum, and (c) O 1s spectrum.

the quasi-spherical morphology indicates the formation process in which the melted $In_2V_2O_7$ at a high pressure and high temperature cools down immediately and nucleates to form $In_2V_2O_7$ nanoparticles. It is also reported in previous investigation on the shock synthesis of materials.[36]

During the shock compression process, the relative density of precursor powder ($\rho_{00}/\rho$) and flyer velocity are the two main parameters to adjust the shock temperature and pressure, respectively. The decrease in $\rho_{00}/\rho$ enhances the adiabatic compression process during shock loading and increases the shock temperature accordingly, which is conducive to promote the synthetic reaction by increasing the activity of the precursor. With the $\rho_{00}/\rho$ at 90%, the XRD patterns of the recovered sample only show two peaks of $In_2V_2O_7$, indicating that the majority of recovered samples (Nos. 1 and 4 samples) are the precursor. As the $\rho_{00}/\rho$ decreases to 40%, the corresponding XRD pattern shows 12 $In_2V_2O_7$ XRD peaks with a higher intensity, indicating that the majority of the recovered sample is $In_2V_2O_7$. Thus, the high shock pressure is one key factor to prepare tetragonal pyrochlore-like $In_2V_2O_7$ in this study.

Moreover, a high pressure is another key factor to synthesize $In_2V_2O_7$. As the flyer velocities increase, the shock pressure increases from 55 GPa (Nos. 1−3 experiments) to 90 GPa (Nos. 4−6 experiments). The corresponding yield of $In_2V_2O_7$ also increases accordingly. Under conditions of a relative density of 40% and a shock pressure of 90 GPa, the yield of $In_2V_2O_7$ is close to 100%. In previous studies, the pressure condition to synthesize $InVO_4$ is usually normal pressure, but the formation pressure of pyrochlore-like transition metal vanadate with a formula of $A_2V_2O_7$ is usually high.

Our study suggests that the shock method possesses high potential to synthesize bimetal oxide nanopowder, especially metastable bimetal oxides. Furthermore, the shock method is an ideal approach for doping and activation of nanopowders, implying the potential one-step synthesis of doped $In_2V_2O_7$ powder in the further investigation.

## CONCLUSIONS

In this study, we obtained novel indium vanadate with a formula of $In_2V_2O_7$ and tetragonal pyrochlore-like structure through a shock-induced chemical reaction. The calculated average XRD parameters of shock-synthesized $In_2V_2O_7$ are listed in Table 4. The crystal size of formed $In_2V_2O_7$ is in the range of 20−30 nm approximately. Our study demonstrates that shock pressure and temperature are the two critical factors to form tetragonal pyrochlore-like $In_2V_2O_7$ nanopowder. The increase in shock pressure and temperature improves the yield of $In_2V_2O_7$. Under conditions at a relative density of 20% and shock pressure of 90 GPa, the yield of $In_2V_2O_7$ is close to 100%. This study proves this feasible approach to synthesize new bimetal oxides with a formula of $A_2B_2O_7$.

**Table 4. XRD Parameters of Formed IVO**

| | $In_2V_2O_7$ | | |
|---|---|---|---|
| peak number | $2\theta$ (°) | $d$ (Å) | $I$ (%) |
| 1 | 14.59 | 6.066 | 8.68 |
| 2 | 29.44 | 3.031 | 49.84 |
| 3 | 31.86 | 2.808 | 100.00 |
| 4 | 36.36 | 2.468 | 52.89 |
| 5 | 39.38 | 2.285 | 21.86 |
| 6 | 46.66 | 1.945 | 6.59 |
| 7 | 53.94 | 1.696 | 30.55 |
| 8 | 59.81 | 1.545 | 21.38 |
| 9 | 61.22 | 1.512 | 6.59 |
| 10 | 62.65 | 1.481 | 22.51 |
| 11 | 66.75 | 1.399 | 6.75 |
| 12 | 77.29 | 1.234 | 7.23 |


https://doi.org/10.1021/acsomega.2c03220
ACS Omega 2022, 7, 27602−27608

## AUTHOR INFORMATION


### Corresponding Author

**Pengwan Chen** − *State Key Laboratory of Explosion Science and Technology, Beijing Institute of Technology, Beijing 100081, China; Advanced Technology Research Institute, Beijing Institute of Technology, Jinan, Shandong 250307, China;* orcid.org/0000-0002-4289-364X; Email: pwchen@bit.edu.cn

### Authors

**Xin Gao** − *State Key Laboratory of Explosion Science and Technology, Beijing Institute of Technology, Beijing 100081, China; Advanced Technology Research Institute, Beijing Institute of Technology, Jinan, Shandong 250307, China;* orcid.org/0000-0003-1308-3063

**Haotian Ran** − *Chongqing Hongyu Precision Industry Group Co., Ltd., Chongqing 402760, China*

**Qiang Zhou** − *China Academy of Ordnance Science, Beijing 100089, China*

**Toshimori Sekine** − *Center for High Pressure Science and Technology Advanced Research, Beijing 100094, China*

**Jianjun Liu** − *State Key Laboratory of Chemical Resource Engineering, Beijing University of Chemical Technology, Beijing 100029, China*

**Yan Chen** − *Advanced Technology Research Institute, Beijing Institute of Technology, Jinan, Shandong 250307, China*

Complete contact information is available at: https://pubs.acs.org/10.1021/acsomega.2c03220


### Notes

The authors declare no competing financial interest.

## ACKNOWLEDGMENTS

This research was supported by the National Natural Science Foundation of China (Grant No. 11521062), the State Key Laboratory of Explosion Science and Technology, Beijing Institute of Technology (Grant No. ZDKT18-01), and the Beijing Institute of Technology Research Fund Program for Young Scholars (Grant No. XSQD-202002004).

## REFERENCES


(1) Errandonea, D.; Garg, A. B. Recent progress on the characterization of the high-pressure behaviour of $AVO_4$ orthovanadates. *Prog. Mater. Sci.* **2018**, *97*, 123−169.

(2) Chu, S.; Sun, H.; Chen, G.; Chen, Y.; Zhou, W.; Shao, Z. Rationally designed water-insertable layered oxides with synergistic effect of transition-metal elements for high-performance oxygen evolution reaction. *ACS Appl. Mater. Interfaces* **2019**, *11*, 25227−25235.

(3) Yin, M.; Bai, X.; Lv, J.; Wu, H.-S. Significant magnetism enhancement and weak spin-orbit coupling effect in $Mn_{13-n}Co_n$ (n = 0-13) bimetal alloy clusters. *J. Magn. Magn. Mater.* **2019**, *481*, 203−211.

(4) Lia, Q. J.; Xia, S. Q.; Wang, X. Y.; Xia, W.; Yu, Y.; Cui, Y. M.; Zhang, J.; Zheng, J.; Cheng, C.; Li, Y. D.; Wang, H.; Huang, S. G.; Wang, C. C. The colossal dielectric properties of $FeNbO_4$. *J. Alloys Compd.* **2014**, *616*, 577−580.

(5) Gardner, J. S.; Gingras, M. J. P.; Greedan, J. E. Magnetic pyrochlore oxides. *Rev. Mod. Phys.* **2010**, *82*, 53−107.

(6) Feng, J.; Xiao, B.; Wan, C. L.; Qu, Z. X.; Huang, Z. C.; Chen, J. C.; Zhou, R.; Pan, W. Electronic structure, mechanical properties and thermal conductivity of $Ln_2Zr_2O_7$ (Ln = La, Pr, Nd, Sm, Eu and Gd) pyrochlore. *Acta Mater.* **2011**, *59*, 1742−1760.

(7) Lang, M.; Zhang, F.; Zhang, J.; Wang, J.; Lian, J.; Weber, W. J.; Schuster, B.; Trautmann, C.; Neumann, R.; Ewing, R. C. Review of $A_2B_2O_7$ pyrochlore response to irradiation and pressure. *Nucl. Instrum. Methods Phys. Res., Sect. B* **2010**, *268*, 2951−2959.

(8) Miyoshi, K.; Nishimura, Y.; Honda, K.; Fujiwara, K.; Takeuchi, J. Magnetic ordering of pyrochlore oxides $R_2Mo_2O_7$ (R=Er−Nd, Y) by AC and DC magnetic measurements. *Phys. B* **2000**, *284-288*, 1463−1464.

(9) Zhang, N.; Li, Q. J.; Huang, S. G.; Yu, Y.; Zheng, J.; Cheng, C.; Wang, C. C. Dielectric relaxations in multiferroic $La_2Ti_2O_7$ ceramics. *J. Alloys Compd.* **2015**, *652*, 1−8.

(10) Li, S.; Hu, J.; Feng, G.; Kong, X.; Jiang, M. Room-temperature ferromagnetism and ferroelectricity of nanocrystalline $La_2Ti_2O_7$. *J. Alloys Compd.* **2010**, *502*, 176−179.

(11) Weber, W. J.; Ewing, R. C. Plutonium Immobilization and Radiation Effects. *Science* **2000**, *289*, 2051−2051.

(12) Dudnik, E. V.; Lakiza, S. N.; Hrechanyuk, N. I.; Ruban, A. K.; Red'ko, V. P.; Hlabay, M. S.; Myloserdov, A. B. The $Gd_2Zr_2O_7$-based materials for thermal barrier coatings. *Powder Metall. Met. Ceram.* **2018**, *57*, 301−315.

(13) Zhong, F.; Zhao, J.; Shi, L.; Xiao, Y.; Cai, G.; Zheng, Y.; Long, J. Alkaline-earth metals-doped pyrochlore $Gd_2Zr_2O_7$ as oxygen conductors for improved $NO_2$ sensing performance. *Sci. Rep.* **2017**, *7*, 4684.

(14) Duan, P.; Han, C.; Zheng, Y.; Cai, G.; Zhong, F.; Xiao, Y. $A_2B_2O_7$ (A= La, Pr, Nd, Sm, Gd and B Ti, Zr, Sn) ceramics for mild-temperature $NO_2$ sensing and reduction. *J. Alloys Compd.* **2020**, *831*, 154866.

(15) Shlyakhtina, A. V.; Pigalskiy, K. S.; Belov, D. A.; Lyskov, N. V.; Kharitonova, E. P.; Kolbanev, I. V.; Borunova, A. B.; Karyagina, O. K.; Sadovskaya, E. M.; Sadykov, V. A.; Eremeev, N. F. Proton and oxygen ion conductivity in the pyrochlore/fluorite family of $Ln_{2-x}Ca_xScMO_{7-\delta}$ (Ln = La, Sm, Ho, Yb; M = Nb, Ta; x = 0, 0.05, 0.1) niobates and tantalates. *Dalton Trans.* **2018**, *47*, 2376−2392.

(16) Shlyakhtina, A. V.; Belov, D. A.; Pigalskiy, K. S.; Shchegolikhin, A. N.; Kolbanev, I. V.; Karyagina, O. K. Synthesis, properties and phase transitions of pyrochlore- and fluorite-like $Ln_2RMO_7$ (Ln = Sm, Ho; R = Lu, Sc; M = Nb, Ta). *Mater. Res. Bull.* **2014**, *49*, 625−632.

(17) Ewing, R. C.; Weber, W. J.; Lian, J. Nuclear waste disposal-pyrochlore ($A_2B_2O_7$) nuclear waste form for the immobilization of plutonium and "minor" actinides. *J. Appl. Phys.* **2004**, *95*, 5949.

(18) Ku, Y.; Wang, L. C.; Ma, C. M. Photocatalytic oxidation of isopropanol in aqueous solution using perovskite-structured $La_2Ti_2O_7$. *Chem. Eng. Technol.* **2007**, *30*, 895.

(19) Gupta, S.; Subramanian, V. Encapsulating $Bi_2Ti_2O_7$ (BTO) with Reduced Graphene Oxide (RGO): An Effective Strategy to Enhance Photocatalytic and Photoelectrocatalytic activity of BTO. *ACS Appl. Mater. Int.* **2014**, *30*, 895−900.

(20) Cao, Y.; Tang, P.; Han, Y.; Qiu, W. Synthesis of $La_2Ti_2O_7$ flexible self-supporting film and its application in flexible energy storage device. *J. Alloys Compd.* **2020**, *842*, 155581.

(21) Mondal, S.; Appalakondaiah, S.; Vaitheeswaran, G. High pressure structural, electronic, and optical properties of polymorphic $InVO_4$ phases. *J. Appl. Phys.* **2016**, *119*, No. 085702.

(22) Joung, M. R.; Kim, J. S.; Song, M. E.; Nahm, S.; Paik, J. H.; Choi, B. H. Formation and microwave dielectric properties of the $Mg_2V_2O_7$ ceramics. *J. Am. Ceram. Soc.* **2009**, *92*, 1621−1624.

(23) Botella, P.; Errandonea, D.; Garg, A. B.; Rodriguez-Hernandez, P.; Muñoz, A.; Achary, S. N.; Vomiero, A. High-pressure characterization of the optical and electronic properties of $InVO_4$, $InNbO_4$, and $InTaO_4$. *SN Appl. Sci.* **2019**, *1*, 389.

(24) Takita, Y.; Hikazudani, S.; Soda, K.; Nagaoka, K. Anaerobic oxidation of isobutane: Catalytic properties of $MgV_2O_6$ and $Mg_2V_2O_7$ prepared by the molten method. *J. Mol. Catal. A* **2008**, *280*, 164−172.

(25) Hase, M.; Matsumoto, M.; Matsuo, A.; Kindo, K. Magnetic properties of the antiferromagnetic spin-1/2 tetramer compound $CuInVO_5$. *J. Phys. Conf. Ser.* **2017**, *969*, No. 012100.

(26) Lundgren, R. J.; Cranswick, L. M. D.; Bieringer, M. In situ X-ray powder diffraction, synthesis, and magnetic properties of $InVO_3$. *J. Solid State Chem.* **2006**, *179*, 3599−3606.
(27) Ye, J.; Zou, Z.; Oshikiri, M.; Matsushita, A.; Shimoda, M.; Imai, M.; Shishido, T. A novel hydrogen-evolving photocatalyst $InVO_4$ active under visible light irradiation. *Chem. Phys. Lett.* **2002**, *356*, 221−226.
(28) Mitoraj, D.; Lamdab, U.; Kangwansupamonkon, W.; Pacia, M.; Macyk, W.; Wetchakun, N.; Beranek, R. Revisiting the problem of using methylene blue as a model pollutant in photocatalysis: The case of $InVO_4/BiVO_4$ composites. *J. Photochem. Photobiol.. A.* **2018**, *366*, 103−110.
(29) Wang, C.; Yang, B.; Liu, H.; Xia, F.; Xiao, J. Potentiometric ammonia sensor with $InVO_4$ sensing electrode. *Sens. Actuators B: Chem.* **2020**, *316*, 128140.
(30) Liu, S.; Hu, F.; Zhang, J.; Tang, H.; Shao, M. Surface-doping effect of $InVO_4$ nanoribbons and the distinctive behavior as gas sensors. *ACS Appl. Mater. Int.* **2013**, *5*, 3208−3211.
(31) Chen, L.; Liu, Y.; Lu, Z.; Zeng, D. Shape-controlled synthesis and characterization of $InVO_4$ particles. *J. Colloids Int. Sci.* **2006**, *295*, 440−444.
(32) Wang, Y.; Cao, G. Synthesis and electrochemical properties of $InVO_4$ nanotube arrays. *J. Mater. Chem.* **2007**, *17*, 894−899.
(33) Enache, C. S.; Lloyd, D.; Damen, M. R.; Schoonman, J.; van de Krol, R. Photo-electrochemical properties of thin-film $InVO_4$ photoanodes: the role of deep donor states. *J. Phys. Chem. C* **2009**, *113*, 19351−19360.
(34) Wang, Y.; Dai, H.; Deng, J.; Liu, Y.; Zhao, Z.; Li, X.; Arandiyan, H. Three-dimensionally ordered macroporous $InVO_4$: fabrication and excellent visible-light-driven photocatalytic performance for methylene blue degradation. *Chem. Eng. J.* **2013**, *226*, 87−94.
(35) Subramanian, M. A. High pressure synthesis of pyrochlore-type manganese vanadate and related compositions. *Mater. Res. Bull.* **1992**, *27*, 939−943.
(36) Ran, H.; Zhou, Q.; Chen, P.; Liu, J.; Sekine, T.; Gao, X. Shock synthesis of nanocrystalline $La_2Ti_2O_7$ powder. *J. Appl. Phys.* **2021**, *130*, 125903.
(37) Arab, A.; Guo, Y.; Zhou, Q.; Chen, P. Fabrication of nanocrystalline AlCoCrFeNi high entropy alloy through shock consolidation and mechanical alloying. *Entropy* **2019**, *21*, 880.
(38) Hillel, G.; Meshi, L.; Kalabukhov, S.; Frage, N.; Zaretsky, E. B. Shock wave characterization of precipitate strengthening of PH 13-8 Mo stainless steel. *Acta Mater.* **2020**, *187*, 176−185.
(39) Guo, Y.; Liu, R.; Arab, A.; Zhou, Q.; Chen, P. Dynamic behavior and adiabatic shearing formation of the commercially pure titanium with explosion-induced gradient microstructure. *Mater. Sci. Eng., A* **2022**, *833*, 142340.
(40) Chen, P.; Gao, X.; Liu, J.; Zhou, Q.; Huang, F. Shock-induced high-concentration nitrogen doping of titania. *Combust., Explos. Shock Waves* **2012**, *48*, 724−729.
(41) Yunoshev, A.; Sil'Vestrov, V. Shock-wave synthesis of novel superhard materials. *Appl. Phys. Lett.* **2001**, *78*, 1385.
(42) Hokamoto, K.; Tomoeda, T.; Fujita, M. Formation of B-C-N heterodiamond through high-temperature shock compression of diamond and c-BN powder mixture. *J. Mater. Sci. Lett.* **2003**, *22*, 1329−1331.
(43) Yin, H.; Chen, P.; Xu, C.; Gao, X.; Zhou, Q.; Zhao, Y.; Qu, L. Shock-wave synthesis of multilayer graphene and nitrogen-doped graphene materials from carbonate. *Carbon* **2015**, *94*, 928−935.
(44) He, H.; Sekine, T.; Kobayashi, T.; Hirosaki, H.; Suzuki, I. Shock-induced phase transition of $\beta$-$Si_3N_4$ to c-$Si_3N_4$. *Phys. Rev. B* **2000**, *62*, 11412−11417.
(45) Gao, X.; Yin, H.; Chen, P.; Liu, J. Shock-induced phase transition of g-$C_3N_4$ to a new $C_3N_4$ phase. *J. Appl. Phys.* **2019**, *126*, 155901.
(46) Jordan, J. L.; Thadhani, N. N. Effect of shock-activation on post-shock reaction synthesis of ternary ceramics. *AIP Conf. Proc.* **2002**, *620*, 1097−1100.
(47) Furukawa, Y.; Sekine, T.; Oba, M.; Kakegawa, T.; Nakazawa, H. Biomolecule formation by oceanic impacts on early Earth. *Nat. Geosci.* **2009**, *2*, 62−66.
(48) Greiner, N. R.; Phillips, D. S.; Johnson, J. D.; Volk, F. Diamonds in detonation soot. *Nature* **1988**, *333*, 440−442.
(49) Xu, C.; Liu, J.; Cui, N.; Chen, P. Shock-induced C-N-S tridoped $TiO_2$ with improved photocatalytic activity under visible light. *J. Mater. Sci. Technol. Res.* **2015**, *2*, 17−24.
(50) Sekine, T.; Zhou, Q.; Chen, P.; Tan, Z.; Ran, H.; Liu, J. Shock synthesis of $Gd_2Zr_2O_7$. *Mater. Res. Proc.* **2019**, *13*, 31−34.
(51) Meyers, M. A., *Dynamic Behavior of Materials*, 1st ed,; Academic Press: New York: Wiley, 1994; pp. 188−211, DOI: 10.1002/9780470172278.


https://doi.org/10.1021/acsomega.2c03220
*ACS Omega* 2022, 7, 27602−27608